

Enhanced adsorption and co-adsorption of heavy metals using highly hydrophilicity amine-functionalized magnetic hydrochar supported MIL-53(Fe)-NH₂: performance, kinetics and mechanism studies

Xin Luo

Chengdu University of Technology

Haiying Du (✉ duhaiying2014@cdut.edu.cn)

Chengdu University of Technology

Xiaochao Zhang

Chengdu University of Technology

Bo Tang

Chengdu University of Technology

Meichen Zhang

Chengdu University of Technology

Hen Kang

Chengdu University of Technology

Yanqi Ma

Chengdu University of Technology

Research Article

Keywords: MOFs, Composite, Invasive plants, Mixed heavy metals, Carbon neutrality

Posted Date: February 2nd, 2023

DOI: <https://doi.org/10.21203/rs.3.rs-2465567/v1>

License: © ⓘ This work is licensed under a Creative Commons Attribution 4.0 International License.

[Read Full License](#)

Version of Record: A version of this preprint was published at Environmental Science and Pollution Research on May 26th, 2023. See the published version at <https://doi.org/10.1007/s11356-023-27740-5>.

Abstract

It is a "kill two birds with one stone" method to convert invasive plants into hydrochar via hydrothermal carbonization as well as coinciding with 3R rules (reduction, recycling and reuse). In this work, a series of hydrochars (pristine, modified and composite) derived from invasive plants *Alternanthera Philoxeroides*(AP) were prepared and applied to the adsorption and co-adsorption of heavy metals (HMs) such as Pb(II), Cr(VI), Cu(II), Cd(II), Zn(II) and Ni(II). The results show MIL-53(Fe)-NH₂- magnetic hydrochar composite (M-HBAP) displayed a strong affinity for HMs, which the maximum adsorption capacity for HMs were 261.74 (Pb(II)), 252.50 (Cr(VI)), 180.92 (Cd(II)), 163.76 (Cu(II)) and 77.84 (Zn(II)) mg/g calculated by Langmuir model. This may be because the doping of MIL-53(Fe)-NH₂ enhanced the surface hydrophilicity of hydrochar, which allows hydrochar to disperse in the water within 0.12 s and possessed excellent dispersibility compared with pristine hydrochar (BAP) and amine-functionalized magnetic modified hydrochar (HBAP). Furthermore, the BET surface area of BAP was improved from 5.63 to 64.10 m²/g after doing MIL-53(Fe)-NH₂. M-HBAP shows a strong adsorption effect on the single HMs system (52-153 mg/g), while it decreased significantly (17-62 mg/g) in the mixed HMs system due to the competitive adsorption. Cr(VI) can produce strong electrostatic interaction with M-HBAP, Pb(II) can react with CaC₂O₄ on the surface of M-HBAP for chemical precipitation, and other HMs can react with functional groups on the surface of M-HBAP for complexation and ion exchange. In addition, five adsorption-desorption cycle experiments and vibrating sample magnetometry (VSM) curves also proved the feasibility of the M-HBAP application.

1. Introduction

Nowadays, the world is facing the challenge of invasive plant encroachment. AP is a malignant invasive species in China. Every year, governments, especially China, spend tens of billions to control the spread of invasive species like AP (Li et al. 2013). What AP brings to mankind is not only environmental damage but also huge economic losses to society. Physical cutting, chemical spraying, biological control and centralized incineration are the traditional methods to eradicate AP (Powell et al. 2013). Due to distinct shortcomings, such as consuming a lot of human and financial resources, causing secondary pollution, and releasing a large amount of CO₂ to contribute to the global greenhouse effect (Powell et al. 2013, Rajapaksha et al. 2015, Weidlich et al. 2020), the disposal methods for the reuse of AP are seriously limited.

According to the 3R strategy and the global carbon reduction goal, it is a "kill two birds with one stone" method to convert AP into high-value materials such as biochar. Research has confirmed biomass can produce a kind of highly aromatic carbon-rich solid material (biochar) after pyrolysis and carbonization under oxygen-limited conditions (Qin et al. 2022). The biochar displayed high stability and its average residence time in the soil can reach 1000 years (Wang et al. 2020). In addition, biochar has been widely used in the fields of water remediation, for it contains a large number of pore structures and rich functional groups and possesses a large specific surface area (S_{BET}) and excellent stability (Lyu et al.

2020, Pan et al. 2021, Thi Thu Nhan et al. 2017). However, due to its hydrophobicity, low adsorption capacity and single composition (Nguyen Thuy Lan et al. 2021, Pandey et al. 2020), the effect of the adsorption capacity of HMs is relatively poor, and the recovery ability in water is also limited (Dissanayake et al. 2020). Except for amino and magnetic modification, which could improve the shortcomings, it is also significant to enhance the dispersibility of the adsorbent. This is because the dispersibility of adsorbents in the liquid phase increases the accessible surface area (Zhang et al. 2009). Wang et al. (Wang et al. 2022) demonstrated that excellent dispersibility greatly increased the adsorption rate and capacity of the adsorbent for bisphenol A. Many methods have been explored to enhance the dispersibility of adsorbents. Zhang et al. (Zhang et al. 2022b) propose a strategy that enhances the dispersion and stability of tetraethylene pentaamine (TEPA) via anchoring TEPA with single site Ni (II) in the pore of the commercial mesoporous silica gel. In addition, in our previous work (Luo et al. 2022), we prepared amino-functionalized magnetic hydrochar derived from invasive plants, which has a good adsorption capacity for Cr(VI) (80.58 mg/g) and has a relatively strong physical stability in aqueous solution, but its poor dispersion in aqueous solution and surface hydrophobicity impel us to further investigate the adsorption and co-adsorption effect of hydrochar-nanoparticle composites on various HMs in aqueous solution.

MIL-53(Fe)-NH₂ (NM-53) possesses flexible ultrahigh porosity and enormous specific surface areas (Fu et al. 2022, Kim et al. 2018), which made it a significant player in wastewater treatment. Despite all this, it has fatal defects in aqueous solution, that is, MOFs are easy to deteriorate, agglomerate and oxidize in aqueous solution (Bhatt et al. 2022), resulting in the inability to give full play to their adsorption capacity. The biochar-based MOFs composites can not only produce a stronger adsorption effect, but also enable MOFs to produce a marked effect more stably in water, and improve the hydrophobicity and agglomeration of biochar in water. Zhu et al. (Zhu et al. 2021) used mushroom waste biochar as the supporting material of magnetic MOFs nanoparticle phase (UIO-66-2COOH), successfully loaded MOFs on biochar and applied it to the adsorption of Sb(III) for 56.49 mg/g. Navarathna et al. (Navarathna et al. 2020) decorated biochar with magnetite magnetic nanoparticles, and then MIL-53-Fe was doped on it to form a dual hybrid and was employed to adsorb and catalytically photodegrade the dye Rhodamine B for 55 mg/g. Up to now, the strategy of enhancing the dispersibility of carbon materials and adsorption ability for single and mixed HMs wastewater via loading of MOFs has not been reported.

In this work, we successfully prepared hydrochar via hydrothermal carbonization (HTC). The hydrochar was amine-functionalized and magnetized and used NM-53 to dope on the surface of HBAP to obtain a highly hydrophilicity MOFs-hydrochar composite. This strategy not only further improves the adsorption capacity of hydrochar regardless it is in the single and mixed HMs contaminated water but also the limitations of the adsorbent in water, such as poor dispersion and agglomeration. Mover importantly, this method makes rational use of invasive plants, realizes the 3R strategy, and achieves carbon sequestration to some extent.

2. Experiment

2.1. Feedstocks and reagents

The AP was collected from the Chengdu University of Technology and was washed with deionized water for 3 times, then it was crushed by a grinder into 60 mesh powder.

2.2. Characterization

The characterization technologies used in this paper and the type and country of the machines are shown in Table S2.

2.3. The preparation of hydrochars

The process of preparing BAP, HBAP and NM-53 mainly referred to previous work (Luo et al. 2022, Zhang et al. 2022a). The specific process is shown in detail in the supplementary materials. To obtain the M-HBAP composites, 2 mmol $\text{NH}_2\text{-H}_2\text{BDC}$ and $\text{FeCl}_3\cdot 6\text{H}_2\text{O}$ were added into a beaker containing 40 mL DMF, then the suspension was sonicated for 15 min until fully dissolved. After that, different masses of HBAP (0.1-1 g) were added into the suspension and kept sonicated for 10 min. The mixture finally was transferred into a 100 mL Teflon-linked autoclave which then was placed into the oven at 150 °C for 12 h. After natural cooling, pour out the supernatant and washed the remaining substances with methanol several times and dried at 70 °C for 24 h and obtained M-HBAP. The specific schematic representation of the strategy for the preparation of M-HBAP was displayed in Scheme. 1.

2.4. Batch sorption experiments

Stock solutions (1.0 g/L) of Cr(VI), Pb(II), Cu(II), Zn(II), Ni(II) and Cd(II) were prepared by dissolving $\text{K}_2\text{Cr}_2\text{O}_7$, $\text{Pb}(\text{NO}_3)_2$, $\text{Cu}(\text{NO}_3)_2$, $\text{Zn}(\text{NO}_3)_2$, $\text{Ni}(\text{NO}_3)_2$ and $\text{Cd}(\text{NO}_3)_2$ in deionized water. An initial evaluation of the sorption ability of the M-HBAP was investigated with batch sorption experiments. Aqueous solutions of 50 mg/L of HMs (50.0 mL) at 25 °C were made to study the effects of pH on HMs adsorption on M-HBAP (50.0 mg), and its initial pH value was adjusted by adding 0.1 M HNO_3 and 0.1 M NaOH solutions. The adsorption process was carried out at 25 °C, 200 rpm and reacted for 24 h. After adsorption, the supernatant of the solution was filtered by a Millipore filter (0.45 μm). The concentration of Cr(VI) in the solution was measured by a UV-vis Spectrophotometer (T6 New Century, China) following 1,5-diphenylcarbazide method, and other HMs solutions were measured by atomic absorption spectrophotometer (GGX-800, China). Other experimental details are shown in the supplementary material.

3. Results And Discussion

3.1. Characterization

3.1.1. XRD and FT-IR

The XRD results are shown in Fig. 1(a), where can find the characteristic peaks of hydrochars were located at 14.8° (110) and 22° (002) (Cai et al. 2019a). The five characteristic diffraction peaks appear at 30.2° (220), 35.5° (311), 43.2° (400), 57.3° (511) and 62.9° (440) were discovered to be the crystal form of $\gamma\text{-Fe}_2\text{O}_3$ (Xiao et al. 2019), respectively. Meanwhile, three reflection peaks were noticed at 9.2° , 10.4° and 18.6° corresponding to the characteristic peaks of NM-53 (Zheng et al. 2018), respectively, which means that M-HBAP was successfully prepared. It also demonstrates that the doping of NM-53 would not wreck the crystal structure of hydrochar. Based on the FTIR spectra (Fig. 1(b)), the characteristic peaks at $3000\text{--}3700\text{ cm}^{-1}$ are related to -OH and -NH (Dong et al. 2011). Several obvious absorption peaks appeared at 1560 cm^{-1} , 1650 cm^{-1} and 1253 cm^{-1} , which could be attributed to C-O and C = O vibration of carboxylic groups (Xiong et al. 2018) and vibrations of amino groups on benzene rings, while the strength at 1375 cm^{-1} and 774 cm^{-1} was observed, which were attributed to C-O (Xiong et al. 2018) and vibration of benzene rings (Gao et al. 2017), indicating that the successful doping of NM-53. Moreover, the peaks at 537 cm^{-1} and 582 cm^{-1} were assigned to Fe-O vibration (Zhao et al. 2021), 1325 cm^{-1} and 1106 cm^{-1} were typical syringyl (S) peaks (Tian et al. 2022), 1415 cm^{-1} was attributed to the vibration of the aromatic skeleton (Son et al. 2018). Moreover, C-H stretching vibration in $-\text{CH}_3$ and $-\text{CH}_2$ (2933 cm^{-1} and 2841 cm^{-1}), C = C and C = N ($1604\text{--}1415\text{ cm}^{-1}$) were also observed (Park et al. 2016, Taha et al. 2016). The stretching of the ionic or chelated carboxylic groups ($-\text{COOMe}$) was found at 1437 cm^{-1} (Yang et al. 2014). These results show that the introduction of NM-53 would enhance the functional groups on M-HBAP, and the abundant functional groups contained on the surface of M-HBAP are conducive to the removal of HMs.

3.1.2. SEM and BET

It can be seen from Fig. 2(a) that M-HBAP displayed rod-like structures with many particles of uniform size covered around and on the surface. These particles were cubic on the M-HBAP surfaces, which are recognized as $\gamma\text{-Fe}_2\text{O}_3$ and NM-53 crystal particles. Such a structure significantly alleviates the pore blocking or fillings, improving ion accessibility (Song et al. 2022), and permitting better mass transfer and diffusion of constituents into the inner iron nanoparticles (Badawi et al. 2021). After the adsorption of HMs, the surfaces of M-HBAP were found to be covered with a layer of flakes, which confirmed that HMs were adsorbed on the surface of M-HBAP. For the co-adsorption of HMs ions, the degree of damage was greater than that of others. As shown in Fig. S2, the surface elements of M-HBAP changed before and after co-adsorption, and HMs elements were found in the EDS spectra after co-adsorption. The abscission phenomenon was found in the SEM images (Fig. S3), in which the skeleton structure of HBAP is directly exfoliated into smaller and asymmetrical rod-like or thin-layer flakes. This may be because the doping of NM-53 wrecked the hydrochar structures during the second hydrothermal reaction, resulting in the abscission of the hydrochar skeleton. This also explains the discovery of many rod-like flakes on the surface of M-HBAP. These results show that the M-HBAP will lose some porous structures during the synthesis process, making it easier for HMs to adhere to it. Moreover, it may also be part of the reason for the enhancement of its dispersion.

The S_{BET} of the M-HBAP was measured to further explore its pore structures. The N_2 adsorption/desorption isotherms were presented in Fig. 1(c), which could be recognized as pseudo-type IV curves. The S_{BET} of M-HBAP is raised by about 6 times and has a higher pore volume compared with HBAP, which makes it easier to undergo ions exchange with HMs and promotes diffusion (Table S6). Before and after the co-adsorption, the S_{BET} of M-HBAP changed dramatically, from 64.10 to 16.20 m^2/g , and so did the pore volume and micropore volume. These phenomena were due to the pore-filling and adsorption of HMs ions over the surface of the M-HBAP (Hassan et al. 2022).

3.1.3 Water contact angle

The change of the water drop angle of different materials (BAP, HBAP and M-HBAP) over time is shown in Fig. 1(d-e). Both BAP and HBAP show obvious hydrophobicity with a CA of over 100° , and not be immersed in the material with the extension of time (0–20 s). Instead, the M-HBAP shows absolute hydrophilicity. Within less than 0.2 s, the CA of M-HBAP is closed to 0° and completely immersed in the surface. This shows that the surface of hydrochar changes from nonpolar to polar. The improvement of hydrophilicity may be attributed to the introduction of more hydrophilicity O-containing functional groups in the secondary hydrothermal reaction (Sun et al. 2019). The above results show that during the preparation of M-HBAP, the loaded NM-53 can transform the hydrophobicity of the surface of hydrochar into hydrophilicity, which is conducive to its full diffusion in HMs solutions, increase its chances of contact with HMs ions, and finally improves the adsorption capacity of HMs.

3.2. Adsorption of HMs in single system

3.2.1. Effect of the additional amount of biochar

M-HBAP synthesized by HBAP with different proportions (0.1–1.5 g) was successfully prepared, which then were applied to the adsorption of Cr(VI) and Pb(II). As shown in Fig. 3(a), with the increased proportion of HBAP, the adsorption capacity of Cr(VI) and Pb(II) was relatively poor when the additional amount was 0.1–0.3 g. In addition, the adsorption capacity reached the maximum when the additional amount of HBAP was 1.0 g. Therefore, 1.0 g was selected as the optimal addition amount for the next adsorption experiment.

3.2.2. Effect of pH

It can be found from Fig. S4 that the optimum pH of HMs adsorption by M-HBAP was 4, 2, 5, 6, 5, 6 corresponding to Cu(II), Cr(VI), Pb(II), Zn(II), Ni(II) and Cd(II), in which the adsorption capacity for Cr(VI) was particularly outstanding (45.52 mg/g). The adsorption capacity for Cu(II) and Pb(II) is close to the maximum when the pH 6, which was attributed to the precipitation of HMs ions. In fact, most of the articles (> 92%) avoided pH > 7 since the formation of insoluble $\text{Pb}(\text{OH})_2$ leads to metal precipitation and inhibits the adsorption process (Vesali-Naseh et al. 2021). Similarly, the complete removal of Cu(II) when pH 6 is largely due to its precipitation effect. Therefore, the optimum pH of Pb(II) and Cu(II) was determined as 5 and 4 in this experiment.

3.2.3. Adsorption kinetics and isotherms

The adsorption kinetic curve and fitting curve of M-HBAP are shown in Fig. 3(b). and Fig. S6. In the first 30 minutes, the adsorption capacity of M-HBAP for HMs increased sharply and the adsorption equilibrium was basically reached at 300 min. The final removal efficiencies followed the order of Pb(II) > Cr(VI) > Cu(II) > Cd(II) > Ni(II) > Zn(II). The adsorption of HMs by M-HBAP has a good fitting effect on the Elovichs model, demonstrating that the removal of HMs by M-HBAP is not a single mechanism, but involves a variety of adsorption mechanisms. To further explore the adsorption behavior of M-HBAP, the intraparticle diffusion model was introduced. As shown in Fig. 3(d) and Table S4, the fitting plot of q_t vs $t^{0.5}$ for HMs contains multiple linear regions, indicating that the adsorption process is governed by a multistep mechanism (Liu & Zhang 2022). The adsorption behaviors of HMs by M-HBAP can be described as three main steps over the whole time range. Stage I (rapid stage, 0–10 min), stage II (slow stage, 10–300 min) and stage III (stable stage, 300–1440 min). In the rapid stage (also called the film diffusion stage), wherein the metal ions are transported from the bulk liquid phase to the adsorbent surface through a film (Neeli et al. 2020), lots of unoccupied active sites on the surface quickly contact with the HMs ions when M-HBAP was just added into the HMs solution, thus leading to the sharp increasing adsorption capacity of M-HBAP for HMs. When most of the active sites on the surface were occupied and the concentration of HMs in the solution decreased, the adsorption of HMs on the M-HBAP reached the slow stage, because only a small amount of HMs ions could contact the unoccupied adsorption sites on the surface of M-HBAP. When all the surface active sites of M-HABP were occupied, it reached a stable period, that is, the adsorption capacity hardly changes.

The adsorption isotherm parameters and the fitting results of the two models are shown in Table S5 and Fig. 3(c). When the concentration of HMs was 500 mg/L, the adsorption tends to equilibrium. The reason for this phenomenon is that with the increase of HMs concentration, the contact probability between M-HBAP and HMs increases, which is directly reflected in the increase of adsorption capacity. The slow increase of adsorption capacity in the later stage is due to the dose of M-HBAP being stationary, and the number of adsorption sites is finite. Although the adsorption capacity of M-HBAP was increased, the residual HMs in the solution were also greatly increased. Therefore, the adsorption rate decreases gradually. The adsorption data were further fitted by the Langmuir model and the Freundlich model (Fig. S8). The Langmuir model is better fitted to M-HABP, indicating that the adsorption process of HMs onto M-HBAP was monolayer adsorption with uniform binding sites, and equal adsorption energies and few interactions between adsorbed species (Li et al. 2020).

3.3. Adsorption of HMs in mixed system

To make this material widely used in industrial wastewater, its adsorption effect in mixed multi-metal solution systems (original pH = 5.12) was explored. As shown in Fig. 3(e), the adsorption capacity of all HMs under mixed conditions for M-HBAP was lower than those under single conditions, suggesting that competitive adsorption between the HMs actively occurred on the surface of the M-HBAP (Lee & Shin 2021). The adsorption capacity of Pb(II) decreased from 153.77 to 55.78 mg/g, which indicates that

competitive adsorption has a serious impact on the adsorption of Pb(II). However, the total adsorption capacity of HMs on M-HBAP has enhanced, which demonstrated that although there existed competitive adsorption, some functional groups (-OH or -NH) on the surface of M-HBAP are enough to undergo cation exchange and complexation reactions (Jung et al. 2018), which relatively improved the adsorption capacity of M-HBAP for HMs. At a relatively low concentration (50 mg/L), the coexisting HMs ions in the solution promote the adsorption of M-HBAP (Fig. 3(f)), and the removal efficiency of Pb(II) and Cu(II) reaches 82% and 78%, followed by Zn(II) (66%), Ni(II) (47%) and Cd(II) (41%), respectively. With the increase of concentration (100–200 mg/L), although the adsorption capacity increases, the removal efficiency also decreases gradually, indicating that a high concentration of coexisting HMs solution could hinder the adsorption ability of M-HBAP, which is consistent with past work (Fan et al. 2021). In addition, Taha et al. (Taha et al. 2016) demonstrated that the adsorption of Pb(II) by adsorbent will be inhibited in the coexistence of Ni(II) and Cd(II), which may be the reason why the removal efficiency of Pb(II) declined so rapidly with increasing concentration of coexisting HMs ions. This may also be related to its adsorption mechanism, that is, M-HBAP shows different adsorption mechanisms in different HMs coexistence systems, thus affecting its adsorption efficiency.

3.4. The mechanism of M-HBAP for removal of HMs

The hydrophilicity of M-HBAP makes it more rapidly immerse and uniformly dispersed in water, making more adsorption sites of M-HBAP contact with HMs. In addition, the improvement of the adsorption capacity of hydrochar is also attributed to the rich functional groups on the surface. Therefore, we analyze the adsorption mechanism of M-HBAP through the characterization of XRD, FT-IR and XPS.

3.4.1. XRD and FT-IR analysis after adsorption

The XRD pattern after the adsorption of HMs is shown in Fig. S9(a). It can be seen that the crystal phase of M-HBAP after the adsorption of Zn(II), Ni(II), Cu(II), Cd(II) and Cr(VI) did not change significantly. The only change was the decline of characteristic peaks intensity, especially the peaks of NM-53, which demonstrated that NM-53 doping on the surface of M-HBAP participated in the adsorption reaction. This result is consistent with the phenomenon observed in the SEM image. Therefore, precipitation or coprecipitation is not the main way for M-HBAP to adsorb Zn(II), Ni(II), Cu(II), Cd(II) and Cr(VI). However, lead oxalate (PbC_2O_4) was found to form on the surface of M-HBAP after adsorbing Pb(II) (JCPDS Card No.14–0803). Calcium oxalate (CaC_2O_4) could form on the surface of hydrochar derived from herbs at low temperatures (100–300°C) (Qian et al. 2016), which explains the formation of PbC_2O_4 on M-HBAP. Meanwhile, the slight shifts and decline of characteristic peaks (-OH, -NH, C = O and C-N) in FT-IR spectra (Fig. S9(b)) of M-HBAP after metal loading also prove that O- and N-containing functional groups have participated in the complexes with HMs. And the peak of -COOMe and C = C decline greatly suggests that ion replacement between Me (K(I), Na(I), Ca(II), Mg(II)) and HMs happened (Yang et al. 2014), and a surface sorption process via functional groups bearing C = C (π -electrons) took place to form cation- π interactions. Therefore, the adsorption of HMs by M-HBAP is chemical bonding adsorption, which is consistent with the adsorption kinetic results.

3.4.2. XPS analysis

The XPS of M-HBAP displayed the following four peaks (Fig. S10): C 1s (72.23%), Fe 2p (2.05%), O 1s (20.46%) and N 1s (5.26%). As shown in Fig. S11(a) and (b), the chemical states of elements of C and N were identified by fitting the peaks of XPS spectra in the C 1s and N 1s regions. The C 1s spectra of M-HBAP were deconvoluted into three peaks at 284.8, 286.02 and 288.62 eV assigned to C-C, C-O and C = O (Xiao et al. 2019). Significant shifts for these peaks to higher binding energies (Table S7) after the adsorption of HMs owing to the interaction between functional groups and HMs on the surface of M-HBAP. For the spectrum of N 1s, the peaks at the junction of 399.17, 400.13 and 400.90 eV are N-H, C = N and N = N (Deng et al. 2017), respectively. The defined N peaks were shifted to higher or lower binding energies, suggesting the shift of the electronic cloud from nitrogen atoms to HMs and the occurrence of chelating between N atoms and HMs (Huang et al. 2018, Li et al. 2022). After adsorption, the content of the N element on the surface of M-HBAP decreased (Table S8), indicating that the chemical bond of the N-containing functional groups broke during the adsorption process. The results of N1s XPS also indicated that HMs are fixed on the surface of M-HBAP by complexing.

After adsorption of HMs, new peaks appeared at the 954.50 and 934.00 eV (Cu 2p), 586.78 and 577.15 eV (Cr 2p), 405.3 and 412.1 eV (Cd 3d), 143.86 and 139.05 eV (Pb 4f) (Fig. S10), which further substantiated the adsorption of Cu(II), Cr(VI), Cd(II) and Pb(II). However, no obvious peaks of Ni 2p and Zn 2p were found in the full spectrum map, which may be because the Zn(II) and Ni(II) were mainly adsorbed into the interior of M-HBAP, so there was less surface adsorption (Sun et al. 2019).

Pb(II), Cd(II), Ni(II), Cu(II) and Zn(II) existed mainly in cationic ion species except for Cr(VI) which mainly existed in anion ion species, therefore the mechanisms of HMs in this study should be distinguished during discussion. The deconvolution of Pb 4f peaks is displayed in Fig. 4(a), which is different from the Pb 4f peaks centered at 144.1 eV and 139.2 eV in the spectra of $\text{Pb}(\text{NO}_3)_2$ (Lian et al. 2020), suggesting that the state of Pb(II) changes when it was adsorbed on the surface of M-HBAP. The Pb 4f_{7/2} spectra were fitted with two peaks at 139.08 eV and 138.72 eV, which could be assigned to PbC_2O_4 and Pb(II), respectively. The existence of typical peaks of PbC_2O_4 and Pb(II) confirms that Pb(II) was adsorbed on M-HBAP, which is consistent with XRD results. The XPS and XRD results suggest that one of the mechanisms of Pb(II) removal by M-HBAP is chemical precipitation. The Cu 2p XPS spectra of M-HBAP samples after copper adsorption is shown in Fig. 4(c). The Cu 2p_{3/2} spectra were deconvoluted into two main peaks at 933.9 and 935.0 eV, which could be assigned to CuO and CuCO_3 . Moreover, the N 1s peak at 400.1 eV was shifted to 400.3 eV corresponding to the peak of Cu-NH, which also confirmed the formation of the Cu-N complex (Tang et al. 2019). Since the optimal adsorption condition of Cu(II) occurs when pH = 4, the mechanism of Cu(II) removal may also be related to H^+ in the solution. Neeli et al. (Neeli et al. 2020) think that one of the mechanisms for Cu(II) removal is ion exchange for H^+ which was adsorbed to the hydroxyl surface groups. The Cd 3d (Fig. 4(d)) existed in two forms at peaks 405.3 and 412.1 eV corresponded to Cd 3d_{3/2} and Cd 3d_{5/2}, respectively. The Cd 3d_{5/2} spectra were fitted with two

peaks at 405.55 and 405.07 eV which could be assigned to $\text{Cd}(\text{OH})_2$ or CdCO_3 . This indicates that cadmium precipitation occurred on the surface of M-HBAP.

The XPS spectrum of Cr 2p (Fig. 4(b)) was deconvoluted into the $2p_{2/3}$ (576.80 and 578.31 eV) and $2p_{1/2}$ (586.44 and 587.70 eV) binding energies, which correspond to the characteristic peaks of the Cr(VI) and Cr(III). This demonstrated that Cr(III) was formed on the surface of M-HBAP, that is, Cr(VI) was reduced to Cr(III) during the adsorption process. Combining the results of N 1s and FT-IR, functional groups play an important role in the reduction process. Cai et al. (Cai et al. 2019b) hold the view that functional groups like C = C and C-OH can act as Lewis bases and provide electrons for the reduction of Cr(VI). At the same time, the electrostatic effect could not be ignored in the adsorption process, for under low pH conditions, the surface of M-HBAP is positively charged, and -NH, -COOH and Fe_2O_3 (Li et al. 2020) can be protonated into $-\text{NH}_2^+$, $-\text{COOH}_2^+$ and FeOH^+ to make Cr(VI) fix on the M-HBAP. More importantly, zeta potential (Fig. S13) shows that the surface of M-HBAP was positively charged, indicating that electrostatic attraction plays an important role during adsorption. The high isoelectric point of M-HBAP may result from the electron donor N-C = O moieties (Betiha et al. 2020).

In conclusion, the obtained M-HBAP has various adsorption mechanisms for different HMs, which was displayed in Scheme. 2.

3.5. Regeneration performance and VSM analysis of M-HBAP

As shown in Fig. S12(a), with the increase of recycle times, the adsorption capacity of M-HBAP for HMs decreased slowly, but its adsorption capacity could still reach 100.56 mg/g, 115.39 mg/g, 40 mg/g, 59.34 mg/g, 72.48 mg/g and 40.15 mg/g which were attributed to Pb(II), Cr(VI), Zn(II), Cu(II), Cd(II) and Ni(II) after the five cycles, which kept 65%, 80%, 43%, 72%, 91% and 73% of the initial adsorption capacity. These results demonstrated that M-HBAP has an excellent regeneration performance, especially for Cd(II), which may be related to its unique adsorption mechanism. The magnetization curve of the M-HBAP was derived with VSM at room temperature. The corresponding VSM curve was shown in Fig. S12(b). The magnetic hysteresis loop shows the S-shaped curve with a saturation magnetization of 24.16 emu/g and without remanence, which was sufficient to be separated from the HMs solution by a permanent magnet. This also suggests that the doping of NM-53 did not destroy the intrinsic magnetism of HBAP. Due to the loading of non-magnetic NM-53 particles, the saturation magnetization of M-HBAP decreased to a certain extent. However, it can also be proved that most of M-HBAP can be collected within 5 s from HMs solution in practical experiments. The excellent regeneration ability and magnetism of M-HBAP could improve the reuse efficiency of the adsorbent. Moreover, Table 1 shows the maximal adsorption capacities (q_m) of M-HBAP for HMs compared with other adsorbents reported in recent works. The adsorption capacity of M-HBAP for HMs was better than other adsorbents to some extent, therefore it has great prospects in the HMs wastewater treatment.

Table 1
Comparison of maximum adsorption capacity for Pb(II), Cu(II), Cd(II), Zn(II), Ni(II) and Cr(VI) with other adsorbents

Adsorbent	HMs	Maximum adsorption capacity	References
Carbon nanomaterial-biochar nanocomposites	Pb(II), Cd(II)	40, 10 mg/g	(Liu et al. 2016)
Biochar-magnetic chitosan composite	Cr(VI)	120 mg/g	(Zhang et al. 2015)
MOF-808-CA	Pb(II)	173.3 mg/g	(Yang et al. 2022)
SAC-bentonite composites	Pb(II), Cd(II)	100.9, 100.8 mg/g	(Niu et al. 2020)
Graphene oxides	Cu(II), Zn(II)	104.2, 95.0 mg/g	(Yao et al. 2020)
Mesoporous silica-polymer	Pb(II), Cu(II), Ni(II)	70.3, 53.45, 40.8 mg/g	(Betiha et al. 2020)
C-phenylcalix[4]pyrogallolarene	Pb(II), Cu(II), Ni(II)	60.9, 8.1, 16.8 mg/g	(Jumina et al. 2020)
Microplastics	Pb(II), Cu(II), Cd(II), Zn(II)	452.5, 152.7, 224.7, 176.1 mg/kg	(Fan et al. 2021)
Zeolite-supported nanoscale zero-valent iron	Cd(II), Pb(II)	48.63, 85.37 mg/g	(Li et al. 2018)
Mesoporous biopolymer hydrogel beads	Pb(II), Cu(II), Cd(II), Ni(II)	21.09, 15.54, 2.47, 2.68 mg/g	(Hassan et al. 2022)
This work	Pb(II), Cu(II), Cd(II), Zn(II), Ni(II), Cr(VI)	261.74, 163.76, 180.92, 77.84, 124.23, 252.50 mg/g	-

4. Conclusion

In conclusion, magnetic hydrochar-MOFs composite with high dispersion and hydrophilicity was successfully prepared by in-situ hydrothermal synthesis and was applied to remove HMs. All HMs adsorption onto M-HBAP followed the Elovichs model and the isotherm was better explained using the Langmuir model. Intraparticle diffusion plots of HMs adsorption involved three main steps corresponding to the fast stage, slow stage and stable stage. In the mixed heavy metal system, the competitive adsorption capacity of M-HBAP was as follows: Pb(II) > Cu(II) > Cd(II) > Zn(II) > Ni(II). Compared with the higher concentration of the mixed HMs solution, M-HBAP shows a better adsorption capacity at low concentrations. The difference in the uptake mechanism of each HMs has been studied using the XPS results. Pb(II) adsorption is mainly removed by coprecipitation on the surface of M-HBAP. The removal of

Cr(VI) mainly involves electrostatic action and reduction reaction. The removal mechanism of other HMs mainly involves complexation reaction, pore filling and ion exchange.

Due to the high cost of MOFs, waste such as electroplating sludge and stainless steel pickling wastewater can be used as raw materials for preparing MOFs in the following work to realize waste recycling for resource conservation without introducing additional toxic chemicals to produce MOFs. Moreover, it is feasible to focus on carbon sequestration and emission reduction and to carry out research on developing hydrochar composite products with high yield, high carbon content and strong stability, and improve the carbon sequestration capacity of hydrochar composite materials.

Declarations

Ethics approval and consent to participate: Not applicable.

Consent for publication: Not applicable.

Authors Contributions: DHY and ZXC contributed to the study conception and design. Material preparation was performed by LX, and data collection and analysis were performed by LX and TB. The first draft of the manuscript was written by LX, and all authors commented on previous versions of the manuscript. ZMC, KH and MYQ contributed to the experiments. All authors read and approved the final manuscript.

Funding: This study was financially supported by the scholars of science and technology activities project of Sichuan province in 2018, supported by Sichuan Science and Technology Program (2021JDRC0105) and Chengdu Science and Technology Program (2022-RC03-00048-CG), the Youth Development Foundation of Chengdu University of Technology in 2021, and State Environmental Protection Key Laboratory of Synergetic Control and Joint Remediation for Soil & Water Pollution (GHBK-2021-007).

Declaration of Competing Interest: The authors declare that they have no competing interests.

Availability of data and materials: Not applicable.

References

1. Badawi AK, Bakhroum ES, Zaher K (2021) Sustainable Evaluation of Using Nano Zero-Valent Iron and Activated Carbon for Real Textile Effluent Remediation. Arab J Sci Eng 46:10365–10380
2. Betiha MA, Moustafa YM, El-Shahat MF, Rafik E (2020) Polyvinylpyrrolidone-Aminopropyl-SBA-15 schiff Base hybrid for efficient removal of divalent heavy metal cations from wastewater. J Hazard Mater 397:122675
3. Bhatt P, Pandey SC, Joshi S, Chaudhary P, Pathak VM, Huang Y, Wu X, Zhou Z, Chen S (2022) : Nanobioremediation: A sustainable approach for the removal of toxic pollutants from the

environment. *Journal of Hazardous Materials* 427

4. Cai W, Wei J, Li Z, Liu Y, Zhou J, Han B (2019a) Preparation of amino-functionalized magnetic biochar with excellent adsorption performance for Cr(VI) by a mild one-step hydrothermal method from peanut hull. *Colloid Surf A-Physicochem Eng Asp* 563:102–111
5. Cai WQ, Wei JH, Li ZL, Liu Y, Zhou JB, Han BW (2019b) Preparation of amino-functionalized magnetic biochar with excellent adsorption performance for Cr(VI) by a mild one-step hydrothermal method from peanut hull. *Colloid Surf A-Physicochem Eng Asp* 563:102–111
6. Deng J, Liu Y, Liu S, Zeng G, Tan X, Huang B, Tang X, Wang S, Hua Q, Yan Z (2017) Competitive adsorption of Pb(II), Cd(II) and Cu(II) onto chitosan-pyromellitic dianhydride modified biochar. *J Colloid Interface Sci* 506:355–364
7. Dissanayake PD, You S, Igalavithana AD, Xia Y, Bhatnagar A, Gupta S, Kua HW, Kim S, Kwon J-H, Tsang DCW, Ok YS (2020) : Biochar-based adsorbents for carbon dioxide capture: A critical review. *Renewable & Sustainable Energy Reviews* 119
8. Dong F, Wu L, Sun Y, Fu M, Wu Z, Lee SC (2011) Efficient synthesis of polymeric g-C₃N₄ layered materials as novel efficient visible light driven photocatalysts. *J Mater Chem* 21:15171–15174
9. Fan T, Zhao J, Chen Y, Wang M, Wang X, Wang S, Chen X, Lu A, Zha S (2021) : Coexistence and Adsorption Properties of Heavy Metals by Polypropylene Microplastics. *Adsorption Science & Technology* 2021
10. Fu H, Wang C-C, Liu W (2022) MOFs for water purification. *Chin Chem Lett* 33:1647–1649
11. Gao Y, Li S, Li Y, Yao L, Zhang H (2017) Accelerated photocatalytic degradation of organic pollutant over metal-organic framework MIL-53(Fe) under visible LED light mediated by persulfate. *Appl Catal B* 202:165–174
12. Hassan M, Naidu R, Du J, Qi F, Ahsan MA, Liu Y (2022) Magnetic responsive mesoporous alginate/beta-cyclodextrin polymer beads enhance selectivity and adsorption of heavy metal ions. *Int J Biol Macromol* 207:826–840
13. Huang X, Cao X, Wang W, Zhong H, Cao Z (2018) Studies on the adsorption behaviors of Pb(II) onto an acyl-thiourea resin. *J Dispers Sci Technol* 39:1316–1323
14. Jumina, Priastomo Y, Setiawan HR, Mutmainah, Kurniawan YS, Ohto K (2020) Simultaneous removal of lead(II), chromium(III), and copper(II) heavy metal ions through an adsorption process using C-phenylcalix[4]pyrogallolarene material. *J Environ Chem Eng* 8:103971
15. Jung K-W, Lee SY, Lee YJ (2018) Hydrothermal synthesis of hierarchically structured birnessite-type MnO₂/biochar composites for the adsorptive removal of Cu(II) from aqueous media. *Bioresour Technol* 260:204–212
16. Kim S-N, Park CG, Huh BK, Lee SH, Min CH, Lee YY, Kim YK, Park KH, Choy YB (2018) Metal-organic frameworks, NH₂-MIL-88(Fe), as carriers for ophthalmic delivery of brimonidine. *Acta Biomater* 79:344–353
17. Lee H-S, Shin H-S (2021) : Competitive adsorption of heavy metals onto modified biochars: Comparison of biochar properties and modification methods. *Journal of Environmental*

18. Li B, Liu J-L, Xu H (2022) Synthesis of polyaminophosphonated-functionalized hydrochar for efficient sorption of Pb(II). *Environ. Sci. Pollut. Res*
19. Li D, Xu L, Zhang Z, Wang Y (2013) The Research Progress on Utilization and Biological Control of *Alternanthera philoxeroides*. *Chin Agric Sci Bull* 29:71–75
20. Li X, Wang C, Zhang J, Liu J, Liu B, Chen G (2020) : Preparation and application of magnetic biochar in water treatment: A critical review. *Science of the Total Environment* 711
21. Li Z, Wang L, Meng J, Liu X, Xu J, Wang F, Brookes P (2018) Zeolite-supported nanoscale zero-valent iron: New findings on simultaneous adsorption of Cd(II), Pb(II), and As(III) in aqueous solution and soil. *J Hazard Mater* 344:1–11
22. Lian Q, Yao L, Ahmad ZU, Gang DD, Konggudinata MI, Gallo AA, Zappi ME (2020) Enhanced Pb(II) adsorption onto functionalized ordered mesoporous carbon (OMC) from aqueous solutions: the important role of surface property and adsorption mechanism. *Environ Sci Pollut Res* 27:23616–23630
23. Liu C, Zhang H-X (2022) : Modified-biochar adsorbents (MBAs) for heavy-metal ions adsorption: A critical review. *Journal of Environmental Chemical Engineering*10
24. Liu T, Gao B, Fang J, Wang B, Cao X (2016) Biochar-supported carbon nanotube and graphene oxide nanocomposites for Pb(II) and Cd(II) removal. *RSC Adv* 6:24314–24319
25. Luo X, Du H, Zhang X, Yang Y (2022) : Amine-functionalized magnetic biochars derived from invasive plants *Alternanthera philoxeroides* for enhanced efficient removal of Cr(VI): performance, kinetics and mechanism studies. *Environ. Sci. Pollut. Res*
26. Lyu H, Zhang Q, Shen B (2020) : Application of biochar and its composites in catalysis. *Chemosphere*240
27. Navarathna CM, Dewage NB, Karunanayake AG, Farmer EL, Perez F, Hassan EB, Mlsna TE, Pittman CU Jr (2020) Rhodamine B Adsorptive Removal and Photocatalytic Degradation on MIL-53-Fe MOF/Magnetic Magnetite/Biochar Composites. *J Inorg Organomet Polym Mater* 30:214–229
28. Neeli ST, Ramsurn H, Ng CY, Wang Y, Lu J (2020) : Removal of Cr (VI), As (V), Cu (II), and Pb (II) using cellulose biochar supported iron nanoparticles: A kinetic and mechanistic study. *Journal of Environmental Chemical Engineering*8
29. Nguyen Thuy Lan C, Anto S, Ahamed TS, Kumar SS, Shanmugam S, Samuel MS, Mathimani T, Brindhadevi K, Pugazhendhi A (2021) : A review on biochar production techniques and biochar based catalyst for biofuel production from algae. *Fuel* 287
30. Niu M, Li G, Cao L, Wang X, Wang W (2020) Preparation of sulphate aluminate cement amended bentonite and its use in heavy metal adsorption. *J Clean Prod* 256:120700
31. Pan X, Gu Z, Chen W, Li Q (2021) : Preparation of biochar and biochar composites and their application in a Fenton-like process for wastewater decontamination: A review. *Science of the Total Environment* 754

32. Pandey D, Daverey A, Arunachalam K (2020) : Biochar: Production, properties and emerging role as a support for enzyme immobilization. *Journal of Cleaner Production* 255
33. Park J-H, Ok YS, Kim S-H, Cho J-S, Heo J-S, Delaune RD, Seo D-C (2016) Competitive adsorption of heavy metals onto sesame straw biochar in aqueous solutions. *Chemosphere* 142:77–83
34. Powell KI, Chase JM, Knight TM (2013) Invasive Plants Have Scale-Dependent Effects on Diversity by Altering Species-Area Relationships. *Science* 339:316–318
35. Qian L, Zhang W, Yan J, Han L, Gao W, Liu R, Chen M (2016) Effective removal of heavy metal by biochar colloids under different pyrolysis temperatures. *Bioresour Technol* 206:217–224
36. Qin F, Li J, Zhang C, Zeng G, Huang D, Tan X, Qin D, Tan H (2022) : Biochar in the 21st century: A data-driven visualization of collaboration, frontier identification, and future trend. *Science of the Total Environment* 818
37. Rajapaksha AU, Vithanage M, Ahmad M, Seo D-C, Cho J-S, Lee S-E, Lee SS, Ok YS (2015) Enhanced sulfamethazine removal by steam-activated invasive plant-derived biochar. *J Hazard Mater* 290:43–50
38. Son E-B, Poo K-M, Chang J-S, Chae K-J (2018) Heavy metal removal from aqueous solutions using engineered magnetic biochars derived from waste marine macro-algal biomass. *Sci Total Environ* 615:161–168
39. Song Y, Song X, Sun Q, Wang S, Jiao T, Peng Q, Zhang Q (2022) Efficient and sustainable phosphate removal from water by small-sized Al(OH)₃ nanocrystals confined in discarded Artemia Cyst-shell: Ultrahigh sorption capacity and rapid sequestration. *Sci Total Environ* 803:150087
40. Sun C, Chen T, Huang Q, Wang J, Lu S, Yan J (2019) Enhanced adsorption for Pb(II) and Cd(II) of magnetic rice husk biochar by KMnO₄ modification. *Environ Sci Pollut Res* 26:8902–8913
41. Taha AA, Shreadah MA, Ahmed AM, Heiba HF (2016) Multi-component adsorption of Pb(II), Cd(II), and Ni(II) onto Egyptian Na-activated bentonite; equilibrium, kinetics, thermodynamics, and application for seawater desalination. *J Environ Chem Eng* 4:1166–1180
42. Tang S, Shao N, Zheng C, Yan F, Zhang Z (2019) Amino-functionalized sewage sludge-derived biochar as sustainable efficient adsorbent for Cu(II) removal. *Waste Manag* 90:17–28
43. Thi Thu Nhan N, Xu C-Y, Tahmasbian I, Che R, Xu Z, Zhou X, Wallace HM, Bai SH (2017) Effects of biochar on soil available inorganic nitrogen: A review and meta-analysis. *Geoderma* 288:79–96
44. Tian Y, Yin Y, Liu H, Zhou H (2022) : One-step hydrothermal carbonization of amine modified black liquor and lignin for efficient Cr(VI) adsorption. *Journal of Water Process Engineering* 46
45. Vesali-Naseh M, Naseh MRV, Ameri P (2021) : Adsorption of Pb (II) ions from aqueous solutions using carbon nanotubes: A systematic review. *Journal of Cleaner Production* 291
46. Wang C, Zhang X, Sun R, Cao Y (2020) : Neutralization of red mud using bio-acid generated by hydrothermal carbonization of waste biomass for potential soil application. *Journal of Cleaner Production* 271

47. Wang P, Pu S, Zhang W, Shi L, Zhang D (2022) : Revisiting the influence of chemical oxidation on the adsorption properties of carbonaceous materials with different structures: Non-dispersible versus dispersible structure. *Separation and Purification Technology* 286
48. Weidlich EWA, Florido FG, Sorrini TB, Brancalion PHS (2020) Controlling invasive plant species in ecological restoration: A global review. *J Appl Ecol* 57:1806–1817
49. Xiao F, Cheng J, Cao W, Yang C, Chen J, Luo Z (2019) Removal of heavy metals from aqueous solution using chitosan-combined magnetic biochars. *J Colloid Interface Sci* 540:579–584
50. Xiong W, Zeng Z, Li X, Zeng G, Xiao R, Yang Z, Zhou Y, Zhang C, Cheng M, Hu L, Zhou C, Qin L, Xu R, Zhang Y (2018) Multi-walled carbon nanotube/amino-functionalized MIL-53(Fe) composites: Remarkable adsorptive removal of antibiotics from aqueous solutions. *Chemosphere* 210:1061–1069
51. Yang B, Xue W, Zhao X, Wang W, Zhu H, Luo L, Huang H, Zhong C (2022) : Synergistic dicarboxylate sites of natural citric acid modified MOF-808 for the deep removal of Pb²⁺ in water. *Journal of Molecular Liquids* 366
52. Yang Y, Wei Z, Zhang X, Chen X, Yue D, Yin Q, Xiao L, Yang L (2014) Biochar from *Alternanthera philoxeroides* could remove Pb(II) efficiently. *Bioresour Technol* 171:227–232
53. Yao N, Li C, Yu J, Xu Q, Wei S, Tian Z, Yang Z, Yang W, Shen J (2020) Insight into adsorption of combined antibiotic-heavy metal contaminants on graphene oxide in water. *Sep Purif Technol* 236:116278
54. Zhang K, Fu Y, Hao D, Guo J, Ni B-J, Jiang B, Xu L, Wang Q (2022a) : Fabrication of CN75/NH₂-MIL-53(Fe) p-n heterojunction with wide spectral response for efficiently photocatalytic Cr(VI) reduction. *Journal of Alloys and Compounds* 891
55. Zhang M-m, Liu Y-g, Li T-t, Xu W-h, Zheng B-h, Tan X-f, Wang H, Guo Y-m, Guo F-y, Wang S-f (2015) : Chitosan modification of magnetic biochar produced from *Eichhornia crassipes* for enhanced sorption of Cr(VI) from aqueous solution. *Rsc Advances* 5, 46955–46964
56. Zhang S, Shao T, Bekaroglu SSK, Karanfil T (2009) The Impacts of Aggregation and Surface Chemistry of Carbon Nanotubes on the Adsorption of Synthetic Organic Compounds. *Environ Sci Technol* 43:5719–5725
57. Zhang S, Chen W, Mu J, Han J, Zhang C, Gao Z, Zhang J, Wang Y, Wang F (2022b) : Single site Ni(II) anchored tetraethylene pentamine for enhancing CO₂ kinetic adsorption rate and long-term cyclic stability. *Chemical Engineering Journal* 436
58. Zhao Q, Xu T, Song X, Nie S, Choi S-E, Si C (2021) : Preparation and Application in Water Treatment of Magnetic Biochar. *Frontiers in Bioengineering and Biotechnology* 9
59. Zheng X-X, Shen L-J, Chen X-P, Zheng X-H, Au C-T, Jiang LL (2018) Amino-Modified Fe-Terephthalate Metal-Organic Framework as an Efficient Catalyst for the Selective Oxidation of H₂S. *Inorg Chem* 57:10081–10089
60. Zhu G, Lin J, Yuan Q, Wang X, Zhao Z, Hursthouse AS, Wang Z, Li Q (2021) : A biochar supported magnetic metal organic framework for the removal of trivalent antimony. *Chemosphere* 282

Schemes

Schemes 1-2 are available in the Supplementary Files section.

Figures

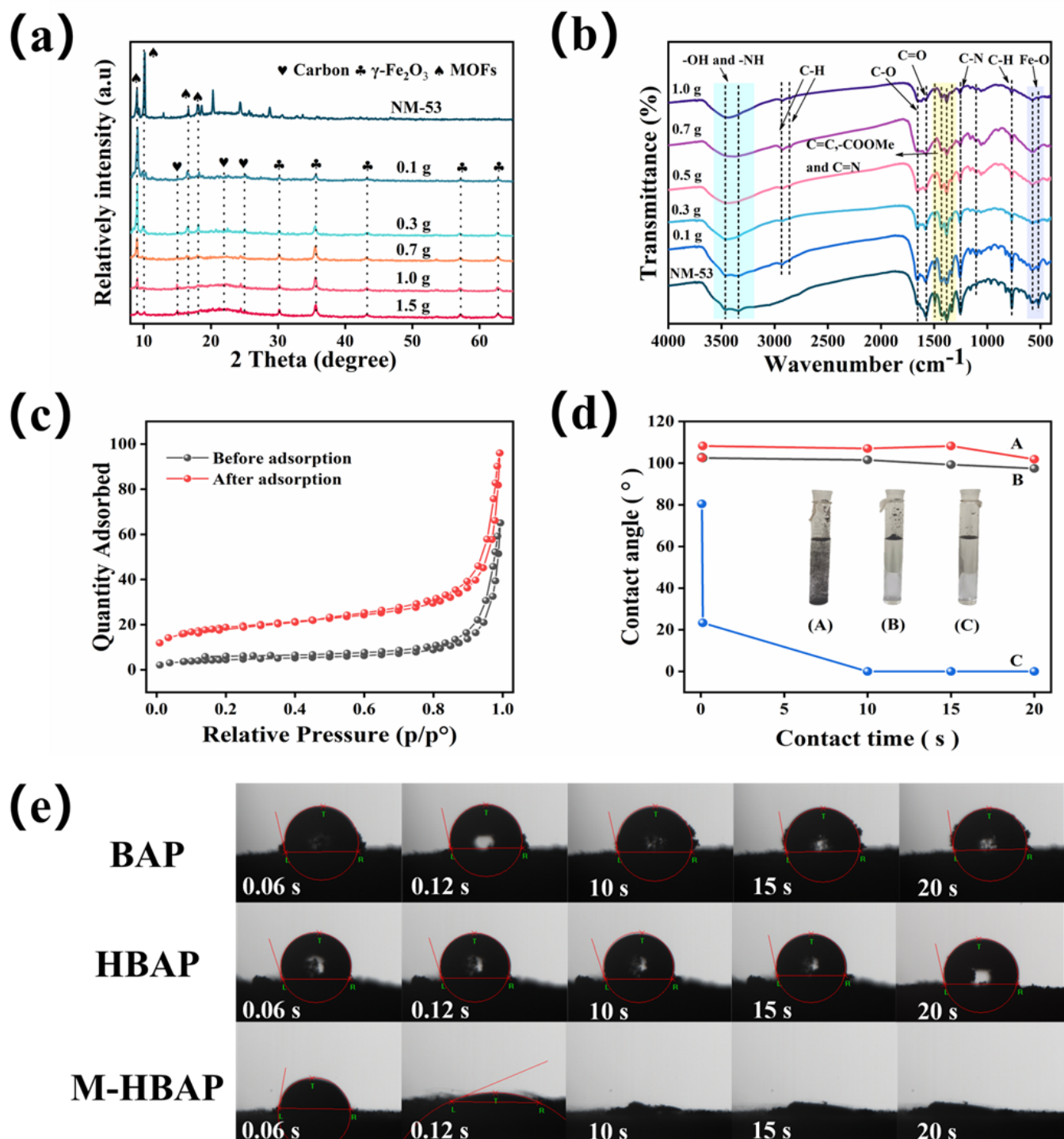


Figure 1

(a) and (b) XRD and FT-IR pattern of NM-53 and M-HBAP with different hydrochar addition ratios; (c) N₂ adsorption-desorption isotherms of M-HBAP before and after co-adsorption; (d-e) The change of water drop angle of different materials over time (A: BAP, B: HBAP and C: M-HBAP).

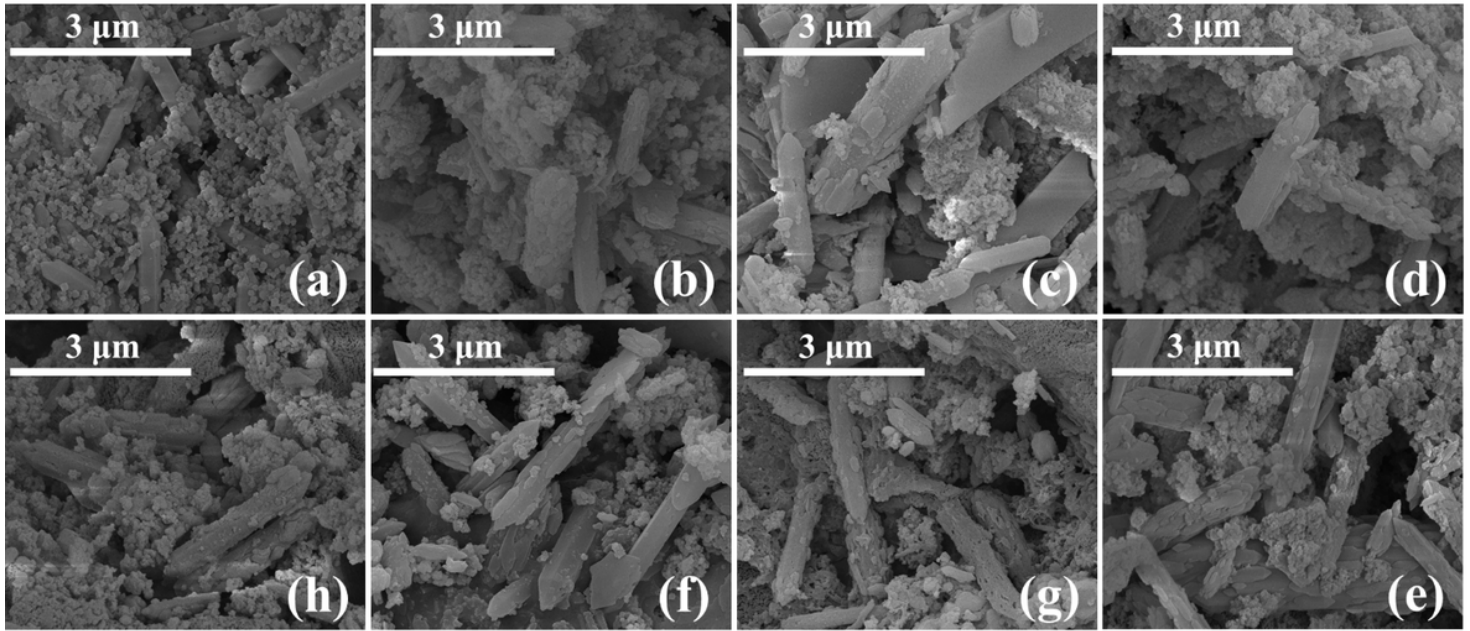


Figure 2

SEM images of (a) M-HBAP, (b)-(g) M-HBAP after Pb(II), Cu(II), Zn(II), Ni(II), Cd(II) and Cr(VI) adsorption, (e) after mixed HMs adsorption.

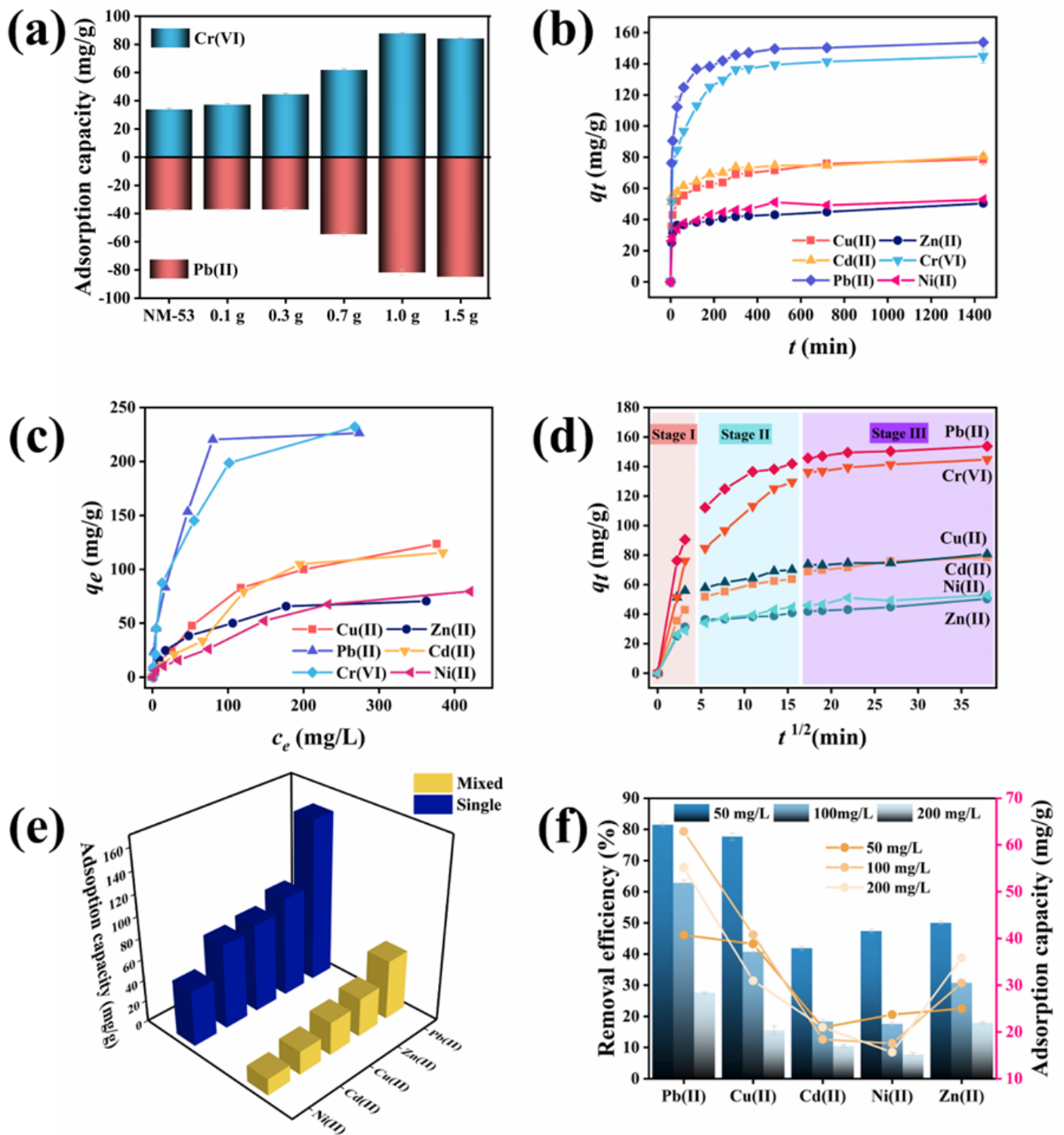


Figure 3

(a) Effects of different HBAP additions on the adsorption of Pb(II) and Cr(VI) by M-HBAP; (b) Adsorption kinetic curve of M-HBAP for HMs; (c) Adsorption isotherm curve of M-HBAP for HMs; (d) Fitting image of intraparticle diffusion model of M-HBAP adsorbing HMs; (e) Comparison of adsorption capacity of M-HBAP for HMs in single HMs and mixed HMs system; (f) Effects of mixed HMs solutions with different concentrations on the adsorption of HMs by M-HBAP.

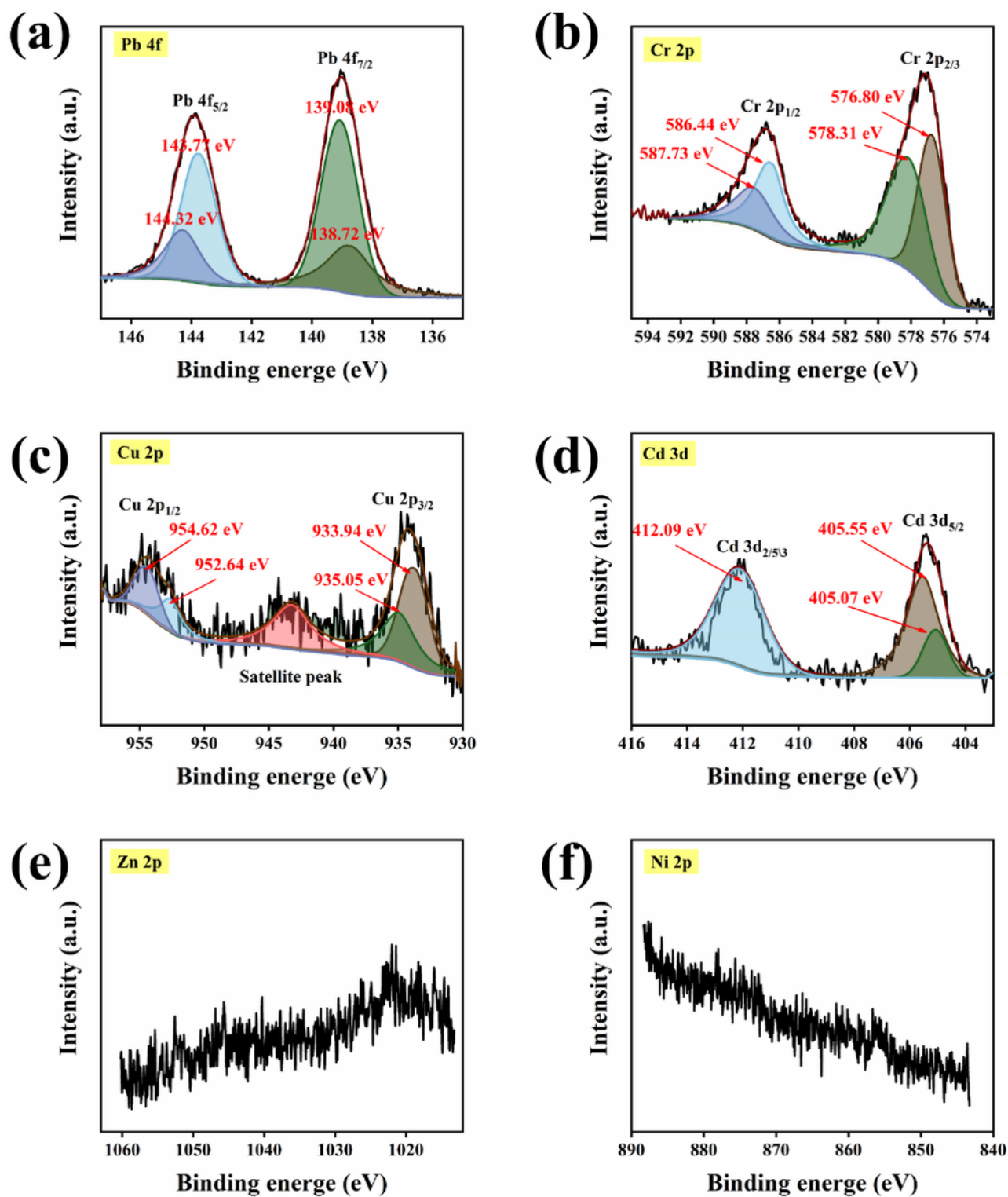


Figure 4

Pb 4f (a), Cr 2p (b), Cu 2p (c) and Cd 3d (d) XPS spectra of MFBAP adsorption of Pb(II), Cr(VI),

Supplementary Files

This is a list of supplementary files associated with this preprint. Click to download.

- [GraphicalAbstract.docx](#)
- [Supplementarydata12.7.docx](#)
- [Scheme1.png](#)
- [Scheme2.png](#)